JPhys Energy

PAPER • OPEN ACCESS

In operando x-ray photoelectron spectroscopy studies of H_2 oxidation and H_2O electrolysis on gadolinia-doped ceria electrodes

Journal of Physics: Energy

PAPER

In operando x-ray photoelectron spectroscopy studies of H_2 oxidation and H_2O electrolysis on gadolinia-doped ceria electrodes

Lei Wang[1,2], **Yi Yu**[3,4], **Karen J Gaskell**[3], **Ethan J Crumlin**[5], **Zhi Liu**[4,5,6], **Bryan W Eichhorn**[3] and **Gregory S Jackson**[7]

[1] Department of Mechanical Engineering, University of Maryland, College Park, MD 20742, United States of America
[2] Redox Power Systems, Beltsville, MD 20705, United States of America
[3] Department of Chemistry and Biochemistry, University of Maryland, College Park, MD 20742, United States of America
[4] School of Physical Science and Technology, ShanghaiTech University, Shanghai 201210, People's Republic of China
[5] Advanced Light Source, Lawrence Berkeley National Laboratory, Berkeley, CA 94720, United States of America
[6] State Key Laboratory of Functional Materials for Informatics, Shanghai Institute of Microsystem and Information Technology, Chinese Academy of Sciences, Shanghai 200050, People's Republic of China
[7] Department of Mechanical Engineering, Colorado School of Mines, Golden, CO 80401, United States of America

E-mail: lei@redoxpowersystems.com **and** gsjackso@mines.edu

OPEN ACCESS

RECEIVED
7 May 2020

REVISED
7 October 2020

ACCEPTED FOR PUBLICATION
21 October 2020

PUBLISHED
18 November 2020

Keywords: in operando, ambient-pressure XPS, solid oxide electrochemical cell, GDC, charge transfer, Ni electrocatalysis

Supplementary material for this article is available online

Abstract

In operando, ambient-pressure x-ray photoelectron spectroscopy (AP-XPS) has been used to evaluate surface states of gadolinia-doped ceria (GDC) thin-film electrodes during H_2 oxidation and H_2O electrolysis, on yttria-stabilized zirconia (YSZ)-supported solid oxide electrochemical cells (SOCs). Porous nickel (Ni) and gold (Au) overlayers deposited on separate GDC thin films served as current collectors and potential electrocatalysts to facilitate heterogeneous chemistry for H_2 oxidation or H_2O electrolysis. Electrochemical characterization of the GDC thin-film electrodes complemented in operando XPS measurements of the O 1s spectra to correlate electrochemical overpotentials with surface chemistry near the Ni/GDC and Au/GDC interfaces. Shifts in O 1s binding energies across the metal/GDC/YSZ interfaces signified changes of local surface potential and provided a means of estimating kinetic parameters associated with charge transfer reactions. Effective oxygen partial pressure and surface potential impacted oxide vacancy and ceria polaron concentrations in the GDC, resulting in different reactivities of the GDC under the tested conditions. Both the Ni/GDC and Au/GDC demonstrated much higher currents for H_2O electrolysis vs. H_2 oxidation for comparable metal/GDC overpotentials due to increased electronic conductivity of the GDC under positive potentials and associated spreading of the electrochemically active region away from the triple-phase boundary. Higher electrochemical activity of the Ni/GDC electrode is attributed to the increased H_2 activation on Ni in promoting charge transfer reactions (particularly for H_2 oxidation). These results provide a basis for developing more informed reaction mechanisms for both H_2 oxidation and H_2O electrolysis of GDC-based composite electrodes in SOCs.

1. Introduction

Solid oxide electrochemical cells (SOCs) offer a means for clean and efficient conversion of chemical energy into electricity as fuel cells or a means of storing excess electrical energy into chemical fuels as electrolysis cells. Gadolinia-doped ceria (GDC) has been investigated widely for its potential as an electrolyte and electrode material in SOCs operating at intermediate temperatures between 500 °C and 700 °C [1–9]. Over this temperature range, GDC has an oxide-ion conductivity that is approximately 1–2 orders of magnitude higher than yttria-stabilized zirconia (YSZ) [2], which has been the most common SOC electrolyte material.

GDC's higher ionic conductivity lowers ohmic resistances associated with bulk-ion transport in SOCs. Under reducing environments associated with the fuel electrode, reduction of some cerium cations (from Ce^{4+} to Ce^{3+}) results in mixed ionic-electronic conductivity (MIEC) [10–12]. The MIEC behaviour lowers open circuit voltages (OCVs) due to electronic leakage, particularly at temperatures above 600 °C, which reduces efficiency in GDC-electrolyte fuel cells. On the other hand, the mixed conductivity enhances catalytic activity in composite metal/GDC electrodes for fuel oxidation (including carbonaceous fuels) and H_2O electrolysis, in part by extending the surface area available for the electrochemical reactions [13–16].

Extensive studies have characterized bulk transport and thermodynamic properties of GDC under conditions relevant for its application as either an electrolyte or a component in a composite SOC fuel electrode [17–20]. Some studies have used thin films to indirectly resolve near-surface oxide vacancies for GDC as a function of effective O_2 partial pressure (P_{O2}) and temperature characteristic of SOC electrodes [21, 22]. Although these studies correlated partial GDC reduction with MIEC behaviour and electrochemical activity due to high concentration of near-surface oxide vacancies, development of reaction mechanisms for GDC-based composite fuel electrodes requires more quantitative surface measurements of GDC in operando with relevant composite materials.

Ambient-pressure x-ray photoelectron spectroscopy (AP-XPS) has received notable attention in recent years for studying high-temperature, electrochemical reactions in operando. Researchers have used this technique to study ceria and doped ceria under low effective P_{O2} characteristic of fuel electrodes in SOCs [14, 15, 23–25]. In operando AP-XPS can measure surface oxidation states associated with electrochemical reactions, as shown in recent noteworthy studies on ceria-based electrodes to explore H_2/H_2O or CO/CO_2 electrochemistry [26–28]. These studies provided insight into the reducibility of ceria surface cations as a function of overpotential, temperature, and gaseous composition. On the other hand, they have not provided significant insight into the interactions between ceria and metal current collectors or within the metal/ceria-based composite electrodes (which can promote catalytic and charge transfer reactions). Understanding metal/GDC interactions is critical for developing quantitative electrochemical mechanisms for GDC-based electrodes such as Ni/GDC composites, which are now being used in intermediate temperature fuel cells. With appropriately designed metal/GDC electrodes, in operando AP-XPS can measure surface potentials and changes in some surface species fractions near the metal/GDC interfaces.

In this study, simultaneous electrochemical measurements and AP-XPS were performed at the Advanced Light Source (ALS) at Lawrence Berkeley National Laboratory on thin-film Ni/GDC and Au/GDC electrodes operating for H_2 oxidation and for H_2O electrolysis [29, 30]. Spatially resolved measurements of the O 1s spectra and binding energy shifts for local surface potentials across the metal/GDC interfaces in combination with simultaneous electrochemical measurements provided critical information on the nature of the electrochemical reactions as a function of temperature and P_{O2} characteristic of fuel electrodes in SOCs. With the increased catalytic activity for Ni compared to Au, differences in the electrochemical performance of the two different electrodes provided an indication on how catalytic activity on the Ni surface can significantly impact the GDC surface chemistry under conditions where reduced electron conductivity confines reactions closer to the metal/GDC interface. The AP-XPS measurements with extensive electrochemical characterization for H_2 oxidation and H_2O electrolysis on the thin-film electrodes at similar operating conditions provided mechanistic insight into the nature or electrochemical reactions across metal/GDC under reducing environments.

2. Experimental

2.1. Electrochemical cell fabrication and mounting

Single-chamber SOCs in this work were fabricated by radio frequency (RF) sputtering (Kurt Lesker PVD 75) of thin-film GDC on polycrystalline YSZ-support substrates. The substrates were made from YSZ powder (Tosoh, 8% by mole of Y_2O_3) pressed in a cylindrical die at 1400 bar. The resulting disk-shape pellet was machined into a square shape with interconnected grooves across the length of one side to provide a location for subsequent deposition of a platinum (Pt) counter electrode (CE) on the opposing side of the GDC thin-film working electrodes (WEs). Figure 1(a) shows how the grooves provided the CE with adequate exposure to gases in the single-chamber cell tests at the AP-XPS facility, where a ceramic contact heater on the CE side controlled the cell operating temperature. The machined-YSZ substrate was sintered at 1450 °C for 3 h to densify with dimensions of 1 mm thick and 10 mm × 10 mm in top-side surface area. The low current density demanded by the thin-film electrodes permitted the use of the thick YSZ electrolyte support. Two 300 nm thick films (2.5 mm × 4.0 mm in area) of GDC (20% by mole of Gd_2O_3, $Gd_{0.2}Ce_{0.8}O_{1.9}$) were deposited by RF-sputtering on the flat topside of the YSZ substrate. The two GDC thin films were separated by a 1.8 mm gap on the YSZ surface to avoid electrochemical interactions during independent electrochemical testing of each WE.

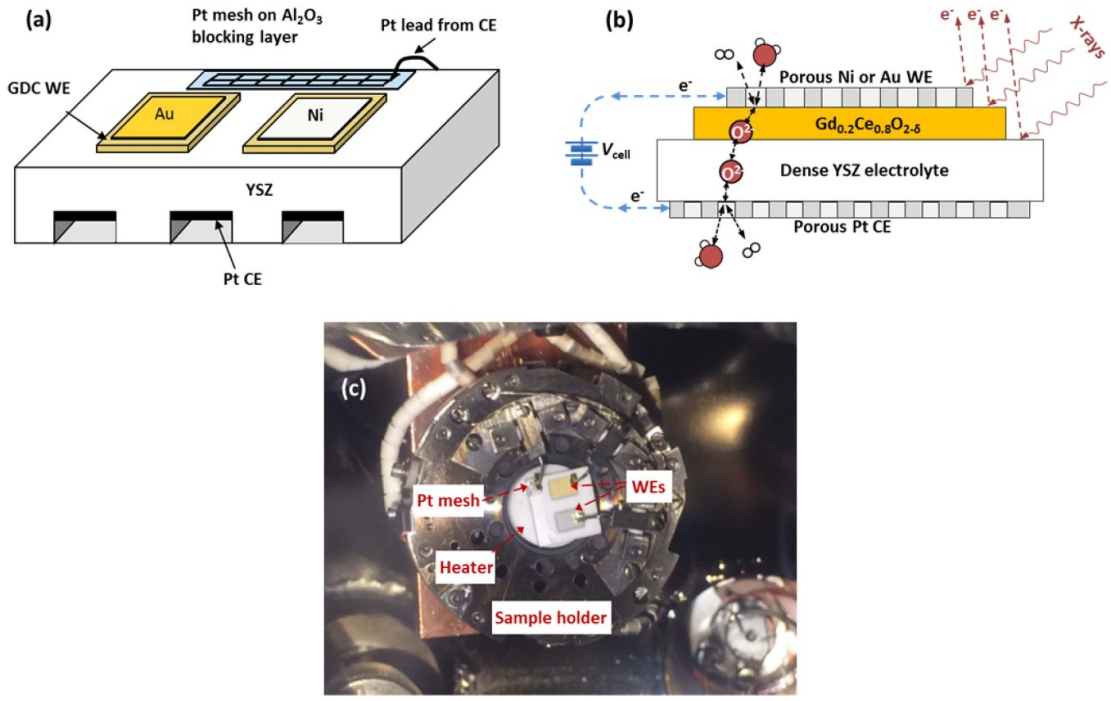

Figure 1. (a) Schematic of YSZ-supported solid oxide electrochemical cell with two thin-film Ni/GDC and Au/GDC working electrodes and a backside Pt counter electrode deposited in grooves of the YSZ. (b) Schematic showing operation of the electrochemical cells at external voltage bias (V_{cell}). For $V_{cell} > 0$, H_2O electrolysis takes place on the Ni/GDC or Au/GDC working electrode (WE) and oxide ions are transported from the WE to the porous Pt counter electrode (CE) where H_2 oxidation occurs. For $V_{cell} < 0$, H_2 oxidation takes place on the Ni/GDC or Au/GDC WE and oxide ions are transported to the WE from the Pt CE where H_2O electrolysis occurs. XPS spectral maps are taken across GDC from the metal/GDC border to the GDC/YSZ border. (c) Photographic image of the WE electrode side of a cell mounted on the ceramic surface heater before AP-XPS testing at the ALS.

Ni and Au (~300 nm thick) metal overlayers were sputter-deposited (AJA International, ATC 1800-V) separately on the two GDC films with a 300 μm border of exposed GDC around the edges of the overlayers. The deposited Ni and Au overlayers were annealed at 750 °C in 5% H_2 in volume (balanced with Ar) such that the overlayers formed interconnected open structure exposing pockets of the GDC surface over the entire area of each WE as illustrated in scanning electronic microscopy (SEM) images for a GDC thin-film WE with a Ni overlayer in figure 2(a) and with an Au overlayer in figure 2(b). The annealed metal overlayers consisted of 1–2 μm wide structures with adequate interconnections to provide both good in-plane conductivity across the thin-film WE and sufficient exposure of the GDC surface for significant length of the triple-phase boundary (TPB) between the metal, GDC, and gas phases on the WE surface. As such, the interconnected Ni and Au overlayers served both as current collectors and as a possible facilitator of charge transfer reactions between the metal and GDC as illustrated in figure 1(b).

The substantial TPB can be characterized by the length per unit geometric area of the GDC surface (L_{tpb}). To characterize the L_{tpb} of both metal/GDC interfaces, scanning electron micrographs, such as those shown in figure 2(a) for the Ni overlayer and figure 2(b) for the Au overlayer, were processed to identify edges of the porous metal overlayer on the GDC surface. Image processing was done in MATLAB and the 'Edge' function was used with the Canny algorithm to detect edges with the porous metal on the GDC surface. In general, the annealing of the two different metal overlayers led to slightly smaller length scales and thus higher L_{tpb} for the Ni overlayer than for the Au. For this study, average L_{tpb} was 1.87×10^6 m for Ni/GDC and 1.23×10^6 m for Au/GDC, per unit surface area (in m^2) of the GDC thin films covered by the Ni or Au overlayer. The 50% higher L_{tpb} for Ni/GDC would improve rates for any rate-limiting reactions involving charge and/or species transfer between the metal and the GDC surface. On the other hand, for reactions occurring completely on the GDC surface, L_{tpb} should play a very limited role in rates.

A 100 nm thick Pt CE was sputter-deposited (AJA International, ATC 1800-V) in the grooves on the backside of the YSZ as shown in figure 1(a). The Pt CE was fired at 800 °C to form a porous overlayer on the YSZ surface and thereby facilitate effective charge transfer for both H_2O electrolysis and H_2 oxidation on the CE. The grooves, in which the Pt was deposited, facilitated gas transport to and from Pt/YSZ/gas TPB on the CE, while allowing the cell to maintain good thermal contact with the surface heater during in operando XPS experiments. A Pt wire was attached to the Pt CE using a Pt paste and brought around to topside of the YSZ where a Pt mesh for electrical contact was fixed on an alumina blocking layer deposited on the topside of the

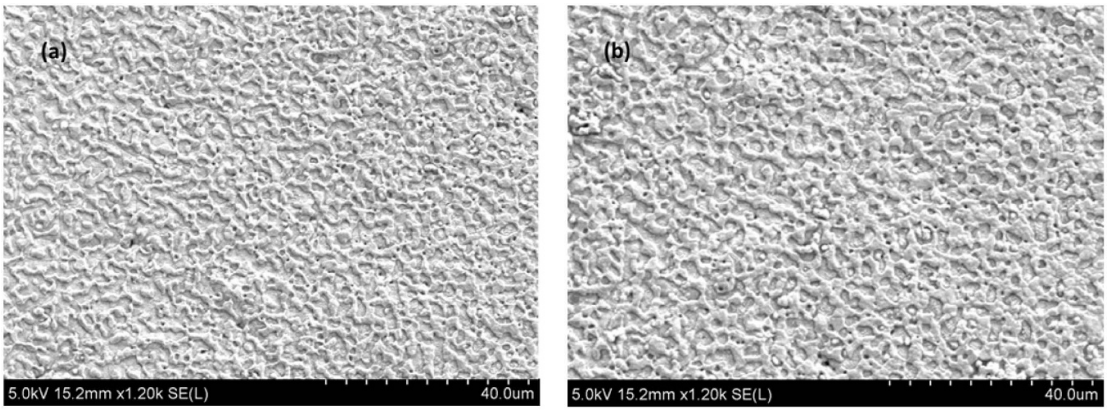

Figure 2. SEM images of surface morphologies of: (a) porous Ni overlayer and (b) porous Au overlayer (sputter-deposited) on thin-film GDC electrode surface after annealing in 5% H_2 in volume (balanced with Ar) at 750 °C.

YSZ substrate to facilitate an external electrical-lead connection. In the AP-XPS test station at ALS, the cell was mounted with three probes pressing separately onto the Ni overlayer, the Au overlayer and the Pt mesh to ensure good electrical connections as well as thermal contact between the backside of the cell and the ceramic heater as shown in figure 1(c).

2.2. Electrochemical characterizations

The SOC was connected to a potentiostat and frequency response analyser, BioLogic at ALS or Metrohm Autolab at the University of Maryland (UMD) for electrochemical characterization. Each WE with the Ni or Au overlayer underwent electrochemical characterization separately. A bias voltage (V_{cell}) was applied between the Pt CE and the connected metal overlayer (Ni or Au), which was grounded. Depending on the sign of the bias, the GDC WE facilitated either H_2 oxidation or H_2O electrolysis while the reverse reaction occurred on the Pt CE. For example, with a positive voltage bias ($V_{cell} > 0$) applied to the cell as illustrated in figure 1(b), oxide ions (O^{2-}) were driven from the GDC WE, where H_2O electrolysis occurred, to the Pt CE, where H_2 was oxidized. On the other hand, a negative bias ($V_{cell} < 0$) drove H_2 oxidation on the GDC WE and H_2O electrolysis on Pt CE.

Electrochemical testing at cell operating temperatures (T) between 570 and 650 °C provided a range of conditions over which the electronic conductivity of GDC rose significantly at the effective P_{O2} in this study. For the ALS measurements, T was determined by the electrolyte bulk resistance (R_{bulk}), which was mapped in calibrated temperature experiments at UMD, where the cell-tube assembly was heated in a temperature-controlled vertical tubular furnace. This was important to the tests at ALS where the beamline test station did not provide direct thermocouple measurements on the cell. Due to limited beamline access at ALS, electrochemical characterization of the SOC at UMD was performed at $P_{tot} = 1$ bar over a broad range of H_2 and H_2O partial pressures (P_{H2} and P_{H2O}) ranging from 2.6 mbar to 26 mbar diluted by an Ar balance. The low P_{H2} and P_{H2O} conditions simulated the pressures available in the AP-XPS facility at ALS.

For the tests at ALS, H_2 ($P_{H2} = 0.26$ mbar) and H_2O ($P_{H2O} = 0.26$ or 0.052 mbar) gases were backfilled into the XPS test chamber through leak valves to the desired composition. P_{H2} and P_{H2O} were monitored via dedicated quadrupole mass spectrometers for each gas, and the measurements were observed to be stable throughout the experiments even during electrochemical activation of the cells. The H_2/H_2O mixtures enabled the GDC WE to perform as a fuel electrode for H_2 oxidation and H_2O electrolysis at different effective P_{O2}.

2.3. X-ray photoelectron spectroscopy measurements

In operando AP-XPS characterization at ALS Beamline 9.3.2 provided quantitative spectroscopic surface chemical analysis [23, 27, 30–34]. The synchrotron-based XPS with differential pumping stages enabled simultaneous electrochemical analysis and surface chemical measurements in the presence of gases up to a few mbar [32]. Effective gas-phase P_{O2} was varied by the P_{H2}/P_{H2O} ratios and the cell operating T. XPS incident radiation fixed at 650 eV permitted measurements of the O 1s spectra with peaks around 532, 534, and 536 eV associated with oxide ion (O^{2-}), surface hydroxyl (OH^-), and near-surface/adsorbed water (H_2O), respectively [15, 35]. At these energy levels, the inelastic mean free path is expected to be approximately 0.65 nm [28], which is only slightly above the GDC lattice constant (0.543 nm).

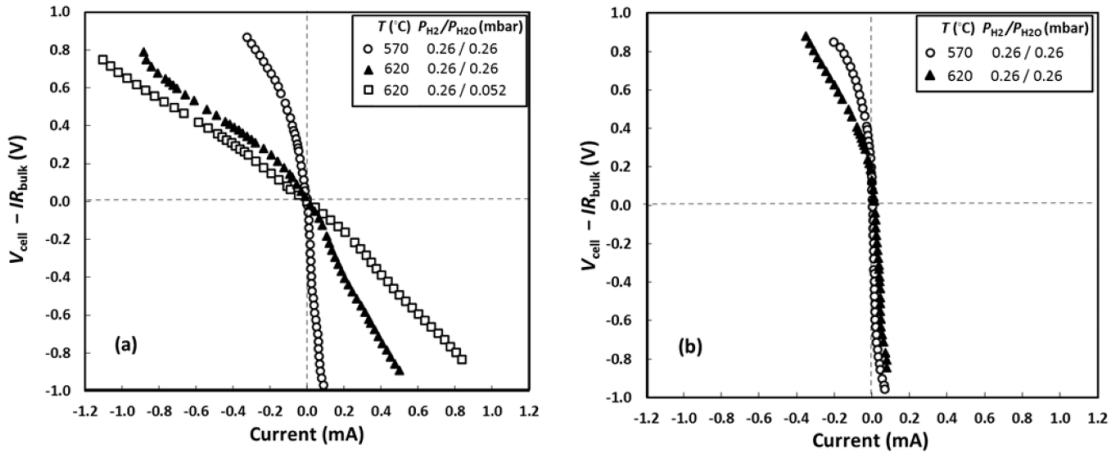

Figure 3. Electrochemical characterization of the thin-film GDC electrochemical cells operating with in operando XPS mapping. IR_{bulk}-corrected V–I curves are plotted for $T = 570$ and 620 °C: (a) Ni/GDC WE operating at different P_{H2}/P_{H2O} ratios and (b) Au/GDC WE operating at $P_{H2}/P_{H2O} = 1.0$.

The beamline is maintained under UHV between periods of ambient pressure operation to reduce risks of contamination. XPS survey scans showed negligibly small C 1s (see supplementary material figure S1 (available online at stacks.iop.org/JPENERGY/3/014004/mmedia)) spectra which verified that there were not significant amounts of carbonaceous surface species. The survey scans up to the 650 eV limit confirmed no significant binding energy shifts resulting from charging effects for relevant elements and valence bands during conditions without any applied voltage bias to the cell. The grounded metal overlayer, in particular the Au current collector, did not show any binding energy shift (on the Au 4f peaks in supplementary material figure S2) and thus served as a reference for assessing the observed binding energy shifts for the O 1s peaks during conditions of applied bias.

Two-dimensional XPS spectral maps (binding energy versus spatial location along a line across the surface of the WE) were recorded with a dispersive hemispherical analyser with two multi-channel plates coupled to a phosphor screen and a charge-coupled device camera installed on the beamline [29]. XPS analyser settings are provided in the supplementary material. The measurements provided spatial resolution of a 16 μm diameter spot size. Linear scans covered a spectral range for the O 1s spectra (525–540 eV) along a line across the exposed GDC from the metal/GDC border to the GDC/YSZ border. Linear scans at different V_{cell} (1.0, 0.6, 0, −0.6, and −1.0 V) provided measurements of surface species and overpotentials for conditions of both H_2O electrolysis and H_2 oxidation on the WE. Analysis of relative shifts of the primary (O^{2-}) and satellite (OH^- and H_2O) peaks in the O 1s spectra associated with V_{cell} provided a basis for determining the local potential at specific location based on binding energy shifts as described in previous AP-XPS studies on solid oxide cells [14, 15].

As for reduction of GDC, past AP-XPS studies [14, 15, 23, 24] have shown changes in the Ce 3d spectra (880–920 eV) to assess the reduction of ceria under operation conditions similar to this study. The Ce 3d peak was beyond the excitation range of the beamline used in this study. As such, we could not readily access the relevant Ce 3d bands and deemed it unnecessary to show Ce 3d spectra in current study. From our previous studies and that of others [36], we provided thermodynamics calculation and analysis of the reduction state of GDC to help explain how the O 1s observations correlated with changes in Ce reduction.

3. Results and discussion

Figures 3(a) and (b) compare the electrochemical performances for the GDC WEs with the Ni overlayer (i.e. Ni/GDC electrode) and with the Au overlayer (i.e. Au/GDC electrode) during in operando XPS measurements at ALS for different T.

The IR_{bulk}-corrected potentials ($V_{cell} - IR_{bulk}$) subtract the ohmic overpotential from V_{cell}, where R_{bulk} is extracted from high-frequency impedance measurements. Because the tests were in a single chamber filled with mixtures of H_2 and H_2O, OCV was very close to 0 V for the H_2/H_2O electrochemistry. Negative $V_{cell} - IR_{bulk}$ (positive/anodic current) indicated H_2 oxidation on the WE whereas positive $V_{cell} - IR_{bulk}$ (negative/cathodic current) indicated H_2O electrolysis on the WE. Since both WEs shared the same YSZ electrolyte support and Pt CE, differences between V–I curves in figures 3(a) and (b) at the same operating

conditions were attributed to differences in electrochemical behaviour of the Ni/GDC and Au/GDC electrodes.

Comparing figures 3(a) and (b) reveals that the Ni/GDC electrode achieved significantly higher current with increasing magnitude of V_{cell}, both for H_2O electrolysis ($V_{cell} > 0$) and particularly for H_2 oxidation ($V_{cell} < 0$). This ratio of currents for large positive and negative V_{cell} is much greater than the 50% increase in L_{tpb} of the Ni/GDC electrode in comparison to the Au/GDC electrode. For H_2O electrolysis, the Ni/GDC electrode shows smaller activation overpotentials at small V_{cell} than the Au/GDC electrode. The Ni/GDC interface enhances charge transfer reaction rates due to the improved ability of Ni to adsorb H and OH on its surface much more effectively than Au [37]. At $P_{H2} = P_{H2O} = 0.26$ mbar and $T = 620$ °C, the Ni/GDC WE supported current densities of -8.7 mA cm^{-2} at $V_{cell} - IR_{bulk} = 0.5$ V and 4.0 mA cm^{-2} at -0.5 V (based on the area of the porous Ni overlayer). At the same conditions, the Au/GDC WE supported current densities of -1.9 mA cm^{-2} at $+0.5$ V and 0.7 mA cm^{-2} at -0.5 V. Under all conditions tested at the ALS, the Ni/GDC maintained significantly higher currents than the Au/GDC electrode with the exception of highly negative cell voltages at the lower $T = 570$ °C where the current densities of Ni/GDC and Au/GDC electrodes are within a factor of 2 which is close to the differences in L_{tpb} per area of the two WEs. The similar performance at highly oxidizing conditions (large negative V_{cell}) may be due to significant build-up of oxygenated species on the Ni surface reducing Ni/GDC charge transfer [38]. Non-oxidized H^+ transfer across the Ni/GDC interface has been assessed to be the principal charge transfer reaction for H_2 oxidation and H_2O electrolysis [39, 40], and the increased affinity for H on Ni surfaces (vs. Au) provides higher exchange current densities and thus, lower activation overpotentials ($\eta_{act,WE}$) for both forward and reverse reactions.

To explore the role of the metal and GDC surfaces on H_2 electrochemical oxidization and H_2O electrolysis, AP-XPS measurements were taken during electrochemical excitations to probe surface states on the metal and GDC as a function of V_{cell}. AP-XPS of electrochemically active surfaces measures shifts in core-level binding energies of specific spectral peaks, which correlates with changes of surface electric potentials [14, 15]. In this study, shifts of the O 1s binding energy spectra across the metal/GDC/YSZ interfaces around the uncoated GDC film border measured changes in surface potentials as a function of V_{cell}. Since the metal electrodes were grounded, the measured binding energy shifts provided measures of $\eta_{act,WE}$ associated with charge transfer reactions across the metal/GDC interface phases. Figures 4(a)–(c) show linear mapping of the relative counts per second (CPS) of the O 1s spectra as a function of position along the Ni/GDC/YSZ border for WEs operating at $P_{H2} = P_{H2O} = 0.26$ mbar and $T = 620$ °C. For highly positive V_{cell} ($= 1.0$ V) in figure 4(a), positive shifts of the O 1s peak on the GDC were small but non-negligible. At these conditions (as discussed further below), the GDC is significantly reduced and thus provides higher polaron concentrations, which facilitates electron transport from as well as H^+ transport to the Ni electrode. On the other hand, much larger negative binding energy shifts with negative V_{cell} (-1.0 V) in figure 4(c) revealed a larger $\eta_{act,WE}$ for a similar current across the Ni/GDC interface, indicating increased transfer resistance for H_2 oxidation (vs. H_2O electrolysis) on the Ni/GDC electrode. At negative V_{cell}, the GDC has lower electronic conductivity and thus likely relies on H^+ surface transport to enhance charge transfer.

The O 1s spectra for each location were fitted to Gaussian/Lorentzian line-shape peaks (GL(30) with a product formula) with Shirley-background corrections using standard XPS data analysis techniques in CasaXPS. The complex peak shapes were fitted with the three peaks related to three oxygen-containing species (O^{2-}, OH^-, and H_2O), exemplified at $V_{cell} = 1.0$ V in figure 4(d). The fits of the overlapping O^{2-} and OH^- peaks assumed identical full widths at half maximum with only a very small variation between the two different electrodes (FWHM(O^{2-}) = FWHM(OH^-) = 1.79 for Ni/GDC and FWHM(O^{2-}) = FWHM(OH^-) = 1.81 for Au/GDC). The integrated percentage area (percentage ratio relative to sum of O^{2-}, OH^- and H_2O areas) for each component was then utilized for estimating surface species fractions. Figures 5(a) and (b) plot fitted O 1s spectra on the GDC surface at three representative V_{cell} and $T = 620$ °C near the Ni/GDC electrode and the Au/GDC electrode, respectively. In general, the local surface concentrations of OH^- and O^{2-} do not change significantly with V_{cell} for either WE, but Ni/GDC shows significantly higher concentration of OH^-, which is likely tied to the higher activities (currents) for both H_2O electrolysis and H_2 oxidation. The higher OH^- occupancy on the GDC can serve as a marker for higher activity because key charge transfer steps in both H_2O electrolysis (reverse direction of reaction R1) and H_2 oxidation (forward direction of reaction R2) as shown here depend on OH^- activity on the GDC surface.

$$H\,(Ni) + O^{2-}\,(O_{GDC}) + Ce^{4+}\,(Ce_{GDC}) \leftrightarrow OH^-\,(O_{GDC}) + Ce^{3+}\,(Ce_{GDC}) + []\,(Ni) + e^-\,(Ni) \qquad (R1)$$

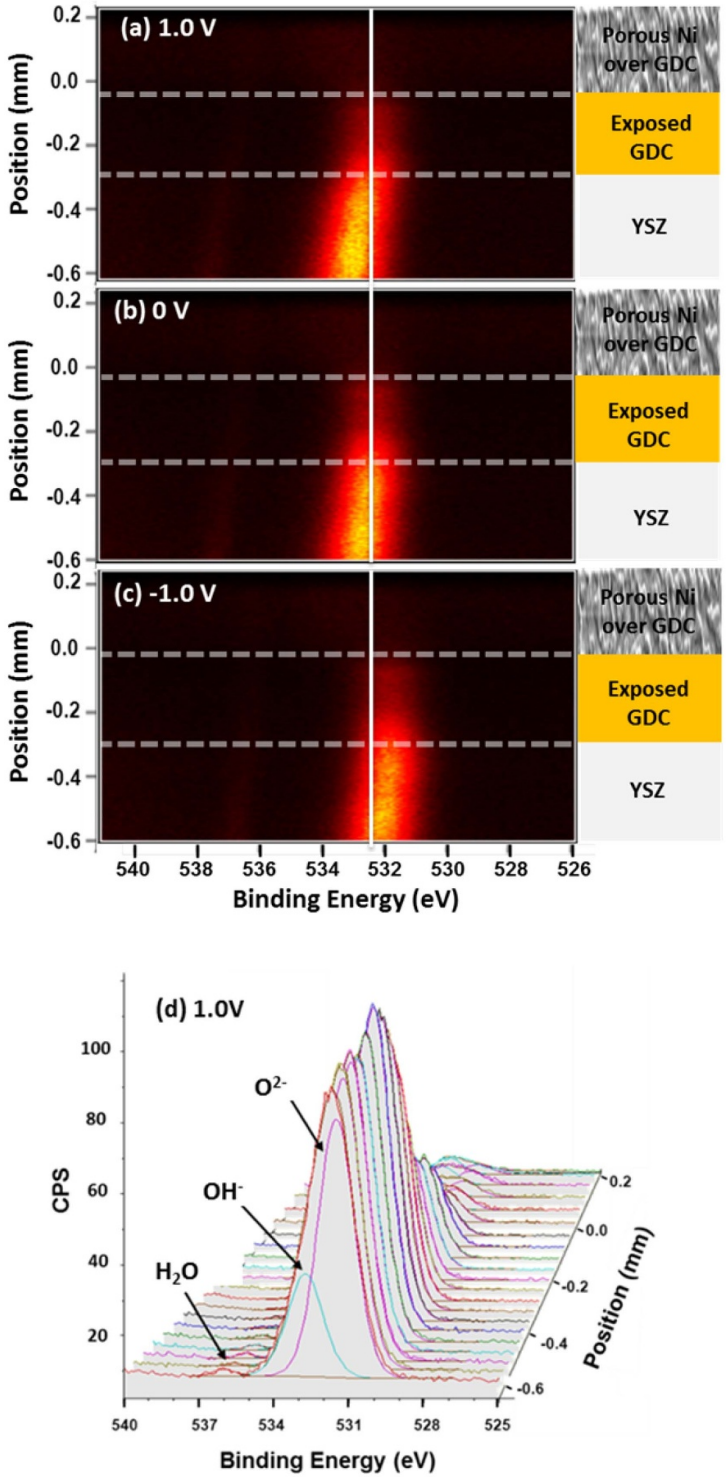

Figure 4. (a)–(c) 2-D mapping of O 1s spectra (with brightness proportional to counts per second). The maps plot spectral intensity vs. binding energy across the exposed Ni/GDC/YSZ edge and show the binding energy shift as a function of V_{cell} associated with local potential change. Plots are shown for cells operating at $P_{H2} = P_{H2O} = 0.26$ mbar and $T = 620$ °C under three potential biases ($V_{cell} = 1.0$, 0, and -1.0 V). (d) Analysis of the O 1s spectra by fitting to Gaussian/Lorentzian line-shapes peaks with Shirley-background corrected in CasaXPS (e.g. $V_{cell} = 1.0$ V). The fitted peaks compose of three oxygen-related species: oxide ion (O^{2-}), surface hydroxyl (OH^-), and near-surface/adsorbed water (H_2O).

$$H\,(Ni) + OH^-\,(O_{GDC}) + Ce^{4+}\,(Ce_{GDC}) \leftrightarrow H_2O\,(O_{GDC}) + Ce^{3+}\,(Ce_{GDC}) + []\,(Ni) + e^-\,(Ni) \qquad (R2)$$

where (O_{GDC}) and (Ce_{GDC}) represent oxide and ceria sites respectively on the GDC surface. The ability for the Ni surface to supply and to receive adsorbed H atoms plays a significant role in enhancing the electrochemical activity of the WE. The weak interactions of adsorbed H_2O with lattice oxygen on the GDC

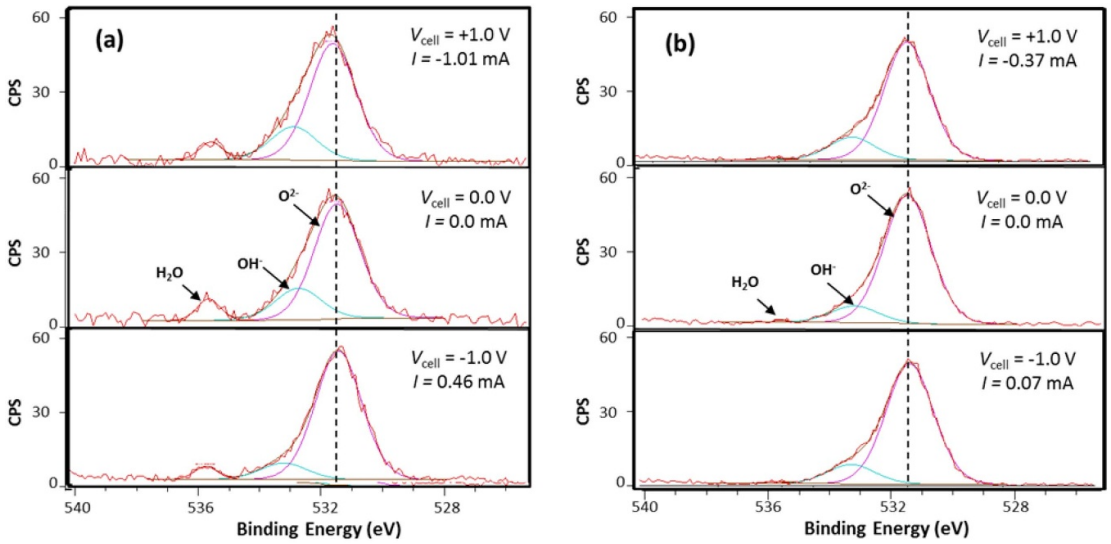

Figure 5. Analyses of the O 1s spectra on GDC surface (close to metal overlayer) with three surface species (O^{2-}, OH^-, and H_2O) under $V_{cell} = 1.0$, 0, and −1.0 V, at $P_{H2} = P_{H2O} = 0.26$ mbar and $T = 620$ °C: (a) Ni/GDC electrode and (b) Au/GDC electrode. Integrated area percentage relative to sum of O^{2-}, OH^- and H_2O areas reflects concentration of each species.

surface [41] implies the importance of the metal surface in providing mobile H species to support more activity on the GDC surface. With the higher affinity of Ni for adsorbing H_2O than Au [41], it is not surprising that the Ni/GDC electrode shows higher intensity for near-surface/adsorbed H_2O in figure 5.

Primary peak (O^{2-}) binding energies after the spectra fitting were plotted as a function of the cell position across the metal/GDC/YSZ border at different V_{cell} as shown in figures 6(a) and (b) for Ni/GDC/YSZ and Au/GDC/YSZ borders, respectively. Binding energy shifts on the GDC surface indicate changes in surface potential associated with the applied bias and resulting reactions. Due to surface charging, shifts in the YSZ surface do not necessarily correspond to surface potentials beneath the GDC film where the O^{2-} charge transfer occurred between those two phases. The relatively flat binding energy distribution across the GDC surface suggests sufficient electronic conductivity to sustain uniform potential distribution on the GDC surface at the measured current densities. Even though the Ni/GDC and Au/GDC WEs have similar magnitudes of $\eta_{act,WE}$ at a given V_{cell}, much higher output currents associated with Ni/GDC electrode indicated superior electrochemical activity of the Ni/GDC electrode. Both WEs showed significantly higher currents for H_2O electrolysis than for H_2 oxidation at similar magnitude of $\eta_{act,WE}$. Plotting $\eta_{act,WE}$ across the metal/GDC interface as a function of current per L_{tpb} (i') in figure 7 shows that for H_2O electrolysis, $\eta_{act,WE}$ for the Au/GDC WE was only slightly higher than for Ni/GDC at the same i'. On the other hand, for H_2 oxidation, $\eta_{act,WE}$ for the Au/GDC WE grew much faster with increasing magnitude of i' than for H_2O electrolysis. This is unlike Ni which had more similar slopes $\eta_{act,WE}$ vs. i' for H_2O electrolysis and H_2 oxidation. Assuming that the two charge transfer reactions R1 and R2 determine the activation overpotential, Zhu *et al* [42] derived the following expression in equation (1) for a relationship between $\eta_{act,WE}$ and i' across the Ni/oxide interface for H_2 oxidation based on the assumption that (R1) is in equilibrium and (R2) is rate limiting.

$$i' = i'_0(T, P_{H2}, P_{H2O})\left[\exp\left(\frac{(1+\beta_{R2})F|\eta_{act,WE}|}{RT}\right) - \exp\left(-\frac{(1-\beta_{R2})F|\eta_{act,WE}|}{RT}\right)\right] \quad (1)$$

where i'_0 is the exchange current density which is a function of T and the partial pressures P_{H2} and P_{H2O} [42]. Fitting equation (1) to measured $\eta_{act,WE}$ plotted in figure 7 provided a basis for estimating fundamental charge transfer parameters such as i'_0 and β_{R2} as shown in table 1. Least squared fits of i'_0 and β_{R2} for H_2O electrolysis currents and for H_2 oxidation currents were performed independently for each WE, and the results in table 1 (which are plotted as curves in figure 7) show that with the exception of H_2 oxidation all fits provide values of β_{R2} close to 0.5. Exchange current densities i'_0 at 620 °C and $P_{H2} = P_{H2O} = 0.26$ mbar are approximately 2.33×10^{-7} A m^{-1} of L_{tpb} with the exception of H_2 oxidation on Au which has an i'_0 that is approximately one order of magnitude lower. While it cannot be presumed that these values represent specific rates of charge transfer reactions, they do provide a basis for estimating orders of magnitudes of specific reaction rate constants that might be used in a more detailed charge transfer reaction rate expression [39, 40].

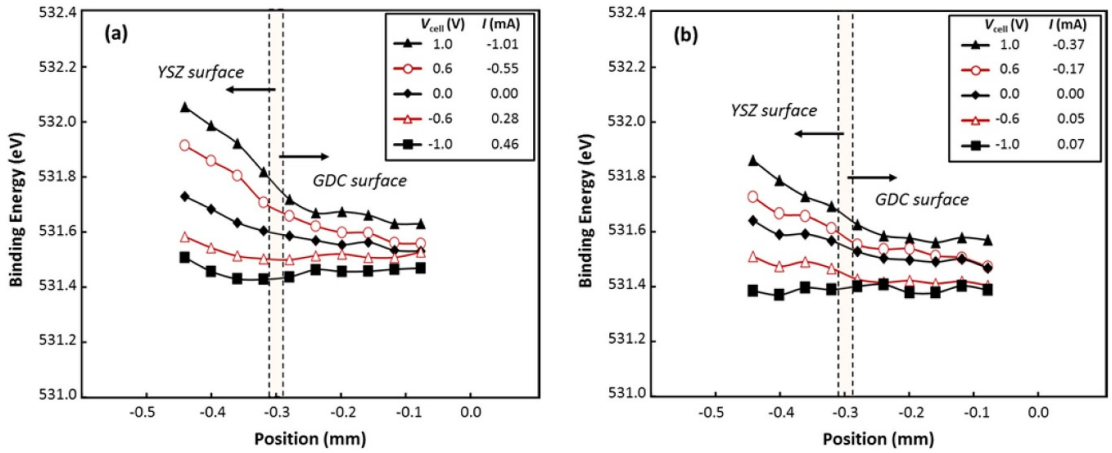

Figure 6. Binding energy of O 1s primary peak (associated with O^{2-}) across the GDC/YSZ interface at $P_{H2} = P_{H2O} = 0.26$ mbar, $T = 620\ ^{\circ}C$: (a) for the Ni/GDC electrode and (b) for the Au/GDC electrode. The shifts of the local binding energy under potential bias relative to the OCV binding energy indicate near-surface electric potential changes.

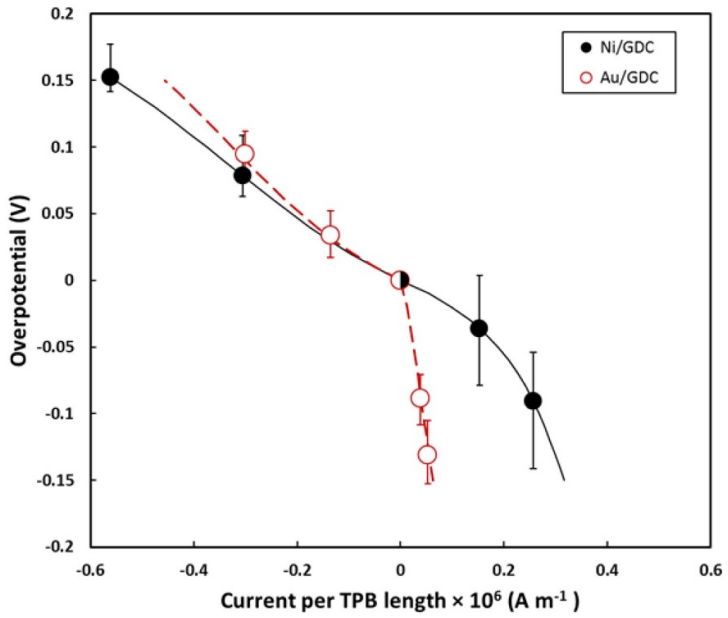

Figure 7. Comparison of measured overpotentials (circular markers) for metal/GDC interface as a function of current per TPB length for both Ni/GDC and Au/GDC electrodes. Overpotentials (with error bars) are determined by the binding energy shifts under different V_{cell} at $P_{H2} = P_{H2O} = 0.26$ mbar and $T = 620\ ^{\circ}C$. The curves represent independent fits of the H_2O electrolysis and H_2 oxidation activation overpotentials for each of the metal/GDC electrodes.

Table 1. Parameters from fits of current per unit length of L_{tpb} to measured metal/GDC activation overpotentials for both Ni/GDC and Au/GDC working electrodes.

	H_2O electrolysis		H_2 oxidation	
Electrode	i'_0 (A m^{-1} of L_{tpb})	β_{R2}	i'_0 (A m^{-1} of L_{tpb})	β_{R2}
Ni/GDC @ 620 °C	2.09×10^{-7}	0.499	2.33×10^{-7}	0.832
Au/GDC @ 620 °C	2.01×10^{-7}	0.570	2.61×10^{-8}	0.542

The charge transfer relationship in equation (1) assumes that the GDC oxide surface is largely equilibrated with the gas phase and that the low effective P_{O2} associated with the H_2/H_2O gas mixtures has not significantly impacted the GDC oxide vacancy site concentrations $[V_O]_L$ and cation site concentrations of reduced ceria polarons $[Ce^{3+}]_L$. Surface oxide vacancies are critical in providing exchange of H_2O with the gas phase through the following surface reactions.

$$H_2O(g) + V_O(O_{GDC}) \leftrightarrow H_2O(O_{GDC}) \quad \text{(R3)}$$

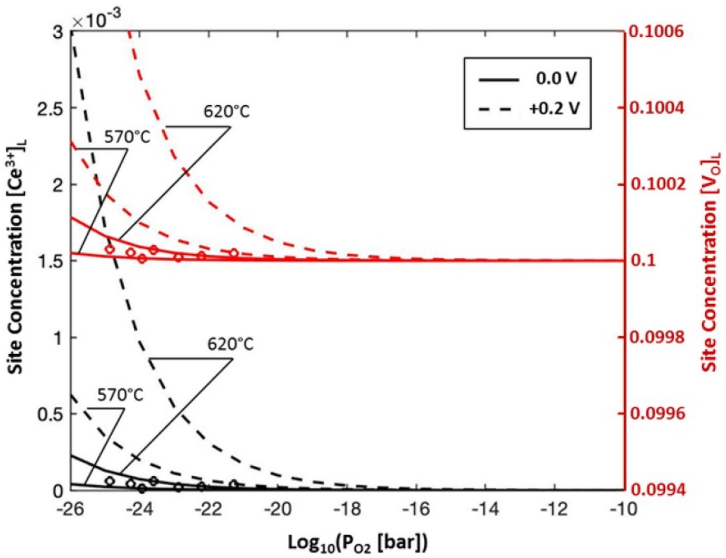

Figure 8. Plot of thermodynamically predicted Ce^{3+} (polaron) site fractions and V_O (oxide vacancy) site fractions as a function of P_{O2} (in bar) for the different test conditions. Solid lines show curves of equilibrium site fractions at $T = 570$ and 620 °C of a given P_{O2} at OCV. Dashed lines shows curves equilibrium site fractions at $T = 570$ and 620 °C of a given P_{O2} and $\eta_{act,WE} = +0.2$ V on the GDC during H_2O electrolysis. Circular markers show equilibrium site fractions of tested conditions (both at ALS and UMD) at OCV.

$$H_2O\,(O_{GDC}) + O^{2-}\,(O_{GDC}) \;\leftrightarrow\; 2OH^-\,(O_{GDC}) \tag{R4}$$

In addition, concentrations of reduced ceria polaron site $[Ce^{3+}]_L$ play a role in increasing electronic conductivity of the GDC and thereby extending the region of effective reaction area for charge transfer reactions [35]. Thus, effective P_{O2} were calculated from chemical equilibrium with the H_2/H_2O mixtures and for the test conditions at the ALS that effective P_{O2} ranged from 1.2×10^{-24} bar at 570 °C to 6.3×10^{-23} bar at 620 °C. A calibrated $Gd_{0.1}Ce_{0.9}O_{1.95}$ defect equilibrium model [36] was adopted for $Gd_{0.2}Ce_{0.8}O_{1.9}$ and used to calculate $[V_O]_L$ and cation site concentrations of reduced ceria polarons $[Ce^{3+}]_L$ to assess whether changes in GDC defect concentrations significantly impact the electrochemical activity under the conditions tested. 20% Gd^{3+} doping on the Ce^{4+} sites results in lower boundary of $[V_O]_L = 0.1$ (out of a maximum of 2) at high P_{O2}. Figure 8 plots the change in $[V_O]_L$ and $[Ce^{3+}]_L$ vs. effective P_{O2} at OCV and at $\eta_{act,WE} = +0.2$ V. Circular markers show predicted $[V_O]_L$ and $[Ce^{3+}]_L$ site fractions of tested conditions (both at ALS and UMD) at OCV. In general, for these relatively low T of solid oxide electrochemical cell operation, at open circuit, the calculated bulk $[V_O]_L$ and $[Ce^{3+}]_L$ remain very close to their fully oxidized limits. While it is understood that surface site concentrations of $[V_O]_L$ and $[Ce^{3+}]_L$ will be much higher [14], those concentrations will likely still close to equilibrated with the bulk and gas phase. On the other hand, when the GDC film experiences potentials $\eta_{act,WE}$, the voltage will shift surface and bulk concentrations as if it experienced a reduction or increase in effective P_{O2} ($P_{O2,eff}$ ($\eta_{act,WE}$)) according to the following equation.

$$P_{O2,eff}\,(\eta_{act,WE}) = P_{O2} \exp\left(-\frac{4F\eta_{act,WE}}{RT}\right) \tag{2}$$

For $\eta_{act,WE} < 0$ during H_2 oxidation at the conditions in this study, the increase in $P_{O2,eff}$ did not significantly impact $[V_O]_L$ and $[Ce^{3+}]_L$, but for $\eta_{act,WE} > 0$ during H_2O electrolysis, the drop in $P_{O2,eff}$ was significant. For an $\eta_{act,WE} = 0.2$ V during H_2O electrolysis will shift the $P_{O2,eff}$ down by a factor of $\sim 10^{-5}$ and thereby increase $[Ce^{3+}]_L$ by a factor of 10 as indicated by the plots for $\eta_{act,WE} = 0.2$ V at the relevant T in figure 8. However, figure 8 also shows that $[V_O]_L$ at these lower T remains close to the high P_{O2} limit. As such, the effects of $\eta_{act,WE}$ on surface chemistry are not likely due to an increase in H_2O exchange but may be due to an extension of the reaction region away from the Ni/GDC electrode TPB through improved electronic conductivity of the more reduced GDC surface. This explains the higher currents for positive $\eta_{act,WE}$ in both the Ni/GDC and Au/GDC electrodes.

To more fully explore the surface chemistry as a function of $\eta_{act,WE}$, the fraction of O 1s peak area attributed to OH^- was evaluated on the GDC surface very near the Ni overlayer. Figure 9 plots the measured

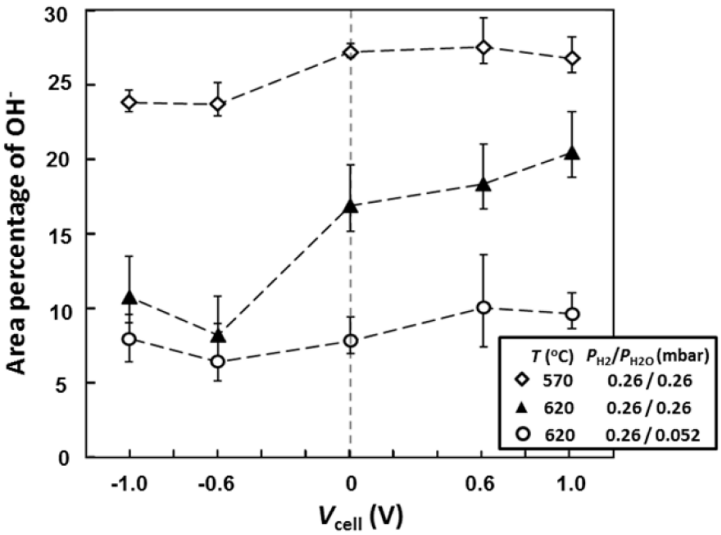

Figure 9. Measured area percentage (with error bars) of OH^- (ratio of integrated OH^- area relative to sum of O^{2-}, OH^- and H_2O areas) on the surface of the GDC near the Ni/GDC interface plotted as function of V_{cell} at different operation conditions at the ALS beamline endstation.

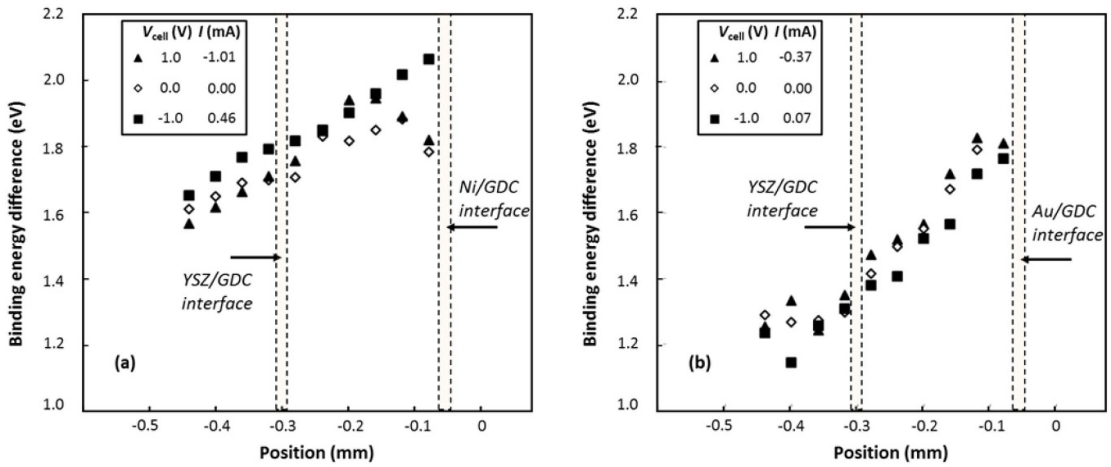

Figure 10. Difference of binding energy shifts between O 1s primary peak (O^{2-}) and secondary peak (OH^-) across: (a) Ni/GDC/YSZ interfaces and (b) Au/GDC/YSZ interfaces, under $V_{cell} = 1.0$, 0, and -1.0 V, at $P_{H2} = P_{H2O} = 0.26$ mbar, and $T = 620\ ^\circ$C.

fraction of the O 1s peak attributed to OH^- which correlates with oxide surface site fractions. Because the AP-XPS detected oxygen a few nm beneath the surface, the surface site fractions of OH^- were likely higher than the area fractions plotted in figure 9. Figure 9 indicates a few interesting trends. Firstly, voltage does not seem to greatly impact the OH^- surface site fractions. Higher water partial pressure (P_{H2O}) and lower T both increased OH^- presence on the surface, but because these values do not represent actual site fractions, it remains unclear if surface OH^- creation or removal remains a rate limiting step. The relative site fractions from figure 9 provide valuable data for surface mechanism calibration relevant for Ni/GDC electrodes in solid oxide electrochemical cell modelling.

Differences between binding energy shifts of OH^- peaks relative to shifts in the O^{2-} peak provided an indicator of electrochemically active region of the oxide surface [28]. Since the OH^- represents exclusively surface adsorbates and a large fraction of the O^{2-} peak comes from subsurface contributions, differences of binding energy shifts between OH^- and O^{2-} correlated with a local potential difference between the surface adsorbates and lattice oxygen in the GDC film during electrochemical reaction. Figures 10(a) and (b) plot the binding energy difference across the metal/GDC/YSZ interfaces at different V_{cell} for both Ni/GDC and Au/GDC, respectively. Under non-zero V_{cell}, no significant differences were seen for the region of exposed GDC surface and YSZ edge compared to OCV. Binding energies of O^{2-} and OH^- shifting by the same amount implies minimal surface charge build-up in that region associated with electrochemistry. At the

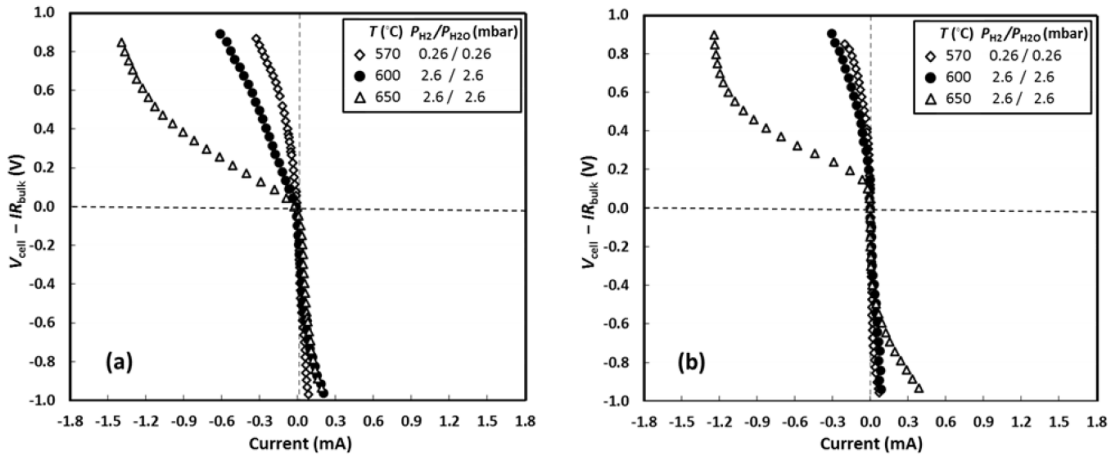

Figure 11. Comparison of electrochemical performance (IR_{bulk}-corrected V–I curves) of the SOCs: (a) Ni/GDC electrode and (b) Au/GDC electrode, at fixed $P_{H2}/P_{H2O} = 1.0$ ratio for T from 570 to 650 °C.

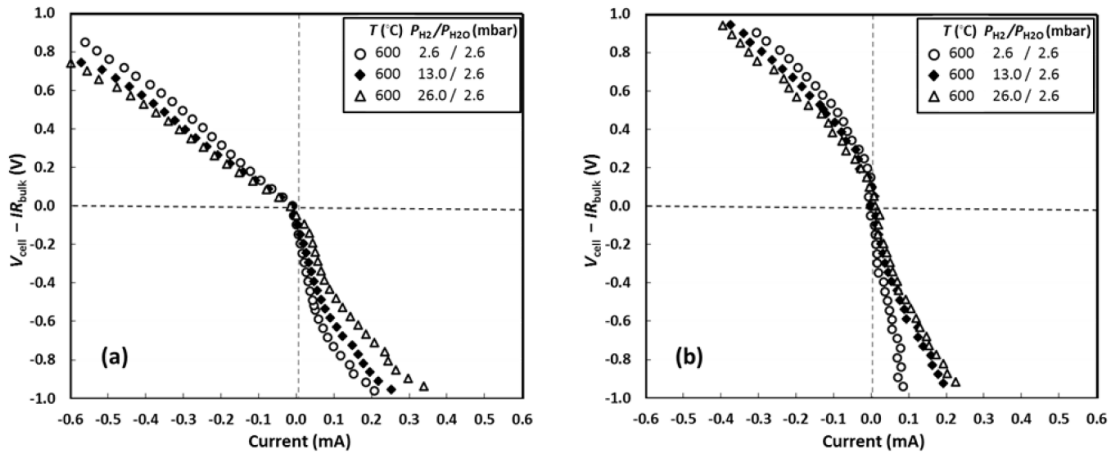

Figure 12. Comparison of electrochemical performance (IR_{bulk}-corrected V–I curves) of the SOCs: (a) Ni/GDC electrode and (b) Au/GDC electrode, for a range of P_{H2}/P_{H2O} ratios at $T = 600$ °C.

metal/GDC interface, the results showed no divergence of binding energy difference except for H_2 oxidation reaction ($V_{cell} = -1.0$ V). This is consistent with the conclusion that surface polarization of the adsorbed OH^- on GDC was minimal when the GDC has higher conductivity (i.e. during electrolysis) or when charge transfer across the metal/GDC interface was low (such as the Au/GDC WE for H_2 oxidation). However, the increased charge transfer reactions at the Ni/GDC interface during H_2 oxidation indicates a significant change in the binding energy difference of OH^- and O^{2-}. This indicates a significant surface charge build-up for ~40–50 μm from the Ni/GDC interface. This suggests the importance of charge transfer reactions R1 and R2 in facilitating electrochemistry and further supports the importance of activity of the metallic component in solid oxide fuel cell anodes [43].

Due to the limited access at the ALS, further electrochemical characterization of the two WEs were performed over a range of T (up to 650 °C) and effective P_{O2} using a range of H_2/H_2O mixtures. A higher range of P_{H2}/P_{H2O} ratios up to 10 were tested, and Ar dilution allowed low P_{H2} and P_{H2O} values to be achieved comparable to those tested at ALS. Similar trends were observed between the Ni/GDC and Au/GDC electrode as shown in figures 11(a) and (b) compared to figures 3(a) and (b), respectively. The IR_{bulk}-corrected V–I curves in figure 11 showed higher currents for H_2O electrolysis for both WEs, but at 600 °C, the Ni/GDC electrode exhibited much lower polarization resistance than the Au/GDC electrode. At the higher $T = 650$ °C where electronic conductivity of the GDC significantly increased, the Au/GDC electrode showed significant increase in electrochemical activity. However, the much lower currents during H_2 oxidation suggests that the negative $\eta_{act,WE}$ suppresses the increased conductivity and associated regions of electrochemical activity. In general, increased reduction of ceria on the GDC surface at higher T and under cathodic current extends the regions of electrochemical activity on the GDC surface, but such effects are suppressed by the negative $\eta_{act,WE}$ during high anodic current.

Dependency on the effective P_{O2} of the electrochemical activity of the Ni/GDC and Au/GDC electrodes was further explored by increasing P_{H2}/P_{H2O} ratios at a constant $T = 600\ ^{\circ}C$. Figures 12(a) and (b) plot IR_{bulk}-corrected V–I curves for both WEs ratios for different P_{H2}/P_{H2O} up to a ratio of 10 (corresponding to an effective $P_{O2} = 10^{-25}$ bar at 600 °C). This lower P_{O2} enables a substantial increase in $[Ce^{3+}]_L$ for positive $\eta_{act,WE}$ as suggested in figure 8, but the improvement in H_2O electrolysis activity is not significant. Nonetheless, the increased reduction more than offsets the increased H_2 product concentration and the higher P_{H2}/P_{H2O} ratios improved H_2O electrolysis activity. Raising the P_{H2}/P_{H2O} ratio more significantly increased activity for H_2 oxidation, particularly for the Ni/GDC electrode. The higher P_{H2}/P_{H2O} ratios reduce the risk for buildup of oxide species on the Ni surface at high anodic current. The improvement of H_2 oxidation on Ni/GDC electrode at higher anodic current provides further proof of the role of the Ni activity on providing a key role in H_2 oxidation for fuel cell conditions.

4. Conclusion

The presented study explored surface potentials, active surface species, and associated electrochemical performance of the Ni/GDC and Au/GDC electrodes in H_2 oxidation and H_2O electrolysis. Ambient pressure XPS measurements of electrochemically active GDC thin-film SOCs provided a means of measuring local surface potential through shift of characteristic binding energy and thereby overpotentials across the metal/GDC interface associated with charge transfer reactions. Specifically, investigation of O 1s core-level XPS of the GDC electrodes under H_2/H_2O atmosphere has revealed how near-surface oxidation states as well as active surface-absorbed species relate to electrochemical activity in this study. Fundamental charge transfer parameters such as i'_0 and β_{R2} were derived to provide a basis for estimating specific reaction rate constants that can be used in a more detailed kinetics. Our study revealed that $[V_O]_L$ and $[Ce^{3+}]_L$ in the GDC were affected by effective P_{O2} and surface potential which significantly impacted the reactivity of the GDC. The relative site fractions of OH^- provided valuable data for surface mechanism calibration relevant for Ni/GDC electrodes. Differences between binding energy shifts of OH^- peaks relative to shifts in the O^{2-} peak revealed the region of electrochemically activity on the GDC away from the Ni/GDC interface.

Further electrochemical characterization of the Ni/GDC and Au/GDC showed the importance of the metal surface activity for increasing H_2 oxidation. The Ni electrode provides much higher H_2 oxidation currents than the less active Au electrode. On the other hand, the increased electronic conductivity of the GDC in ceria reduction-promoted voltages decreased the importance of the Ni activity, and both the Ni/GDC and Au/GDC electrodes showed similar and higher electrochemical activity for H_2O electrolysis. The simultaneous electrochemical measurements and surface characterization with XPS has provided key data to assist in developing a more mechanistic understanding of GDC electrodes for both solid oxide fuel cells and solid oxide H_2O-electrolysis cells.

Acknowledgments

This work was funded through the support of the Office of Naval Research through Contract # N000140510711 (Dr. Michele Anderson program manager). The Advanced Light Source is supported by the Director, Office of Science, Office of Basic Energy Sciences, of the U.S. Department of Energy under Contract # DE-AC02-05CH11231. We thank the University of Maryland Nanocenter and the University of Maryland Energy Research Center (UMERC) for support. We would also like to thank Dr. Chunjuan Zhang (now at BASF) who helped with the sputter deposition of the GDC films and the thin-film current collectors, and Drs. Sandrine Ricote and Huayang Zhu (Colorado School of Mines) who provided valuable feedback on the GDC kinetics.

ORCID iDs

Lei Wang https://orcid.org/0000-0002-7133-7300
Ethan J Crumlin https://orcid.org/0000-0003-3132-190X
Gregory S Jackson https://orcid.org/0000-0002-8928-2459

References

[1] Mogensen M, Sammes N M and Tompsett G A 2000 Physical, chemical and electrochemical properties of pure and doped ceria *Solid State Ion.* **129** 63–94
[2] Steele B C H and Heinzel A 2001 Materials for fuel-cell technologies *Nature* **414** 345–52
[3] Jiang S P and Chan S H 2004 A review of anode materials development in solid oxide fuel cells *J. Mater. Sci.* **39** 4405–39
[4] Wachsman E D and Lee K T 2011 Lowering the temperature of solid oxide fuel cells *Science* **334** 935–9

[5] Lee K T, Gore C M and Wachsman E D 2012 Feasibility of low temperature solid oxide fuel cells operating on reformed hydrocarbon fuels *J. Mater. Chem.* **22** 22405–8
[6] Blackburn B M, Bishop S, Gore C, Wang L, Correa L, Langdo T, Deaconu S and Pan K 2018 *Final Technical Report: Affordable, High-Performance, Intermediate Temperature Solid Oxide Fuel Cells* (https://doi.org/10.2172/1420977)
[7] Green R D, Liu C C and Adler S B 2008 Carbon dioxide reduction on gadolinia-doped ceria cathodes *Solid State Ion.* **179** 647–60
[8] Gaudillere C, Navarrete L and Serra J 2014 Syngas production at intermediate temperature through H2O and CO2 electrolysis with a Cu-based solid oxide electrolyzer cell *Int. J. Hydrogen Energy* **39** 3047–54
[9] Lo Faro M, Zignani S, Trocino S, Antonucci V and Arico A 2019 New insights on the co-electrolysis of CO2 and H2O through a solid oxide electrolyser operating at intermediate temperatures *Electrochim. Acta* **296** 458–64
[10] Atkinson A, Baron S A and Brandon N P 2004 AC impedance spectra arising from mixed ionic electronic solid electrolytes *J. Electrochem. Soc.* **151** E186–93
[11] Joo J H and Choi G M 2007 Electrical conductivity of thin film ceria grown by pulsed laser deposition *J. Eur. Ceram. Soc.* **27** 4273–7
[12] Nakayama M, Ohshima H, Nogami M and Martin M 2012 A concerted migration mechanism of mixed oxide ion and electron conduction in reduced ceria studied by first-principles density functional theory *Phys. Chem. Chem. Phys.* **14** 6079–84
[13] Nakamura T, Kobayashi T, Yashiro K, Kaimai A, Otake T, Sato K, Mizusaki J and Kawada T 2008 Electrochemical behaviors of mixed conducting oxide anodes for solid oxide fuel cell *J. Electrochem. Soc.* **155** B563–69
[14] DeCaluwe S C *et al* 2010 In situ characterization of ceria oxidation states in high-temperature electrochemical cells with ambient pressure XPS *J. Phys. Chem.* C **114** 19853–61
[15] Zhang C J *et al* 2010 Measuring fundamental properties in operating solid oxide electrochemical cells by using in situ X-ray photoelectron spectroscopy *Nat. Mater.* **9** 944–9
[16] Chueh W C, Hao Y, Jung W and Haile S M 2012 High electrochemical activity of the oxide phase in model ceria-Pt and ceria-Ni composite anodes *Nat. Mater.* **11** 155–61
[17] Wang S R, Kobayashi T, Dokiya M and Hashimoto T 2000 Electrical and ionic conductivity of Gd-doped ceria *J. Electrochem. Soc.* **147** 3606–9
[18] Steele B C H 2000 Appraisal of Ce1-yGdyO2-y/2 electrolytes for IT-SOFC operation at 500 degrees C *Solid State Ion.* **129** 95–110
[19] Ruiz-Trejo E and Maier J 2007 Electronic transport in single crystals of Gd-doped ceria *J. Electrochem. Soc.* **154** B583–87
[20] Genreith-Schriever A and De Souza R 2016 Field-enhanced ion transport in solids: reexamination with molecular dynamics simulations *Phys. Rev.* B **94** 224304
[21] Wang S R, Inaba H, Tagawa H, Dokiya M and Hashimoto T 1998 Nonstoichiometry of Ce0.9Gd0.1O1.95-x *Solid State Ion.* **107** 73–79
[22] Bishop S R, Duncan K L and Wachsman E D 2009 Surface and bulk oxygen non-stoichiometry and bulk chemical expansion in gadolinium-doped cerium oxide *Acta Mater.* **57** 3596–605
[23] Chueh W C, McDaniel A H, Grass M E, Hao Y, Jabeen N, Liu Z, Haile S M, McCarty K F, Bluhm H and El Gabaly F 2012 Highly enhanced concentration and stability of reactive Ce3+ on doped CeO2 surface revealed in operando *Chem. Mater.* **24** 1876–82
[24] Papaefthimiou V, Niakolas D, Paloukis F, Teschner D, Knop-Gericke A, Haevecker M and Zafeiratos S 2017 Operando observation of nickel/ceria electrode surfaces during intermediate temperature steam electrolysis *J. Catal.* **352** 305–13
[25] Feng Z, Gopal C, Ye X, Guan Z, Jeong B, Crumlin E and Chueh W 2016 Origin of overpotential-dependent surface dipole at CeO2-x/gas interface during electrochemical oxygen insertion reactions *Chem. Mater.* **28** 6233–42
[26] Feng Z, Machala M and Chueh W 2015 Surface electrochemistry of CO2 reduction and CO oxidation on Sm-doped CeO2-x: coupling between Ce3+ and carbonate adsorbates *Phys. Chem. Chem. Phys.* **17** 12273–81
[27] Wang J *et al* 2019 Threshold catalytic onset of carbon formation on CeO2 during CO2 electrolysis: mechanism and inhibition *J. Mater. Chem.* A **7** 15233–43
[28] Zhang C J *et al* 2013 Mechanistic studies of water electrolysis and hydrogen electro-oxidation on high temperature ceria-based solid oxide electrochemical cells *J. Am. Chem. Soc.* **135** 11572–9
[29] Grass M E *et al* 2010 Ambient pressure XPS for spatial and angular resolution of operational heterogeneous catalysts and electrochemical systems *Abstr. Pap. Am. Chem. Soc.* **240** 1
[30] Crumlin E J, Bluhm H and Liu Z 2013 In situ investigation of electrochemical devices using ambient pressure photoelectron spectroscopy *J. Electron Spectrosc. Relat. Phenom.* **190** 84–92
[31] Grass M E, Karlsson P G, Aksoy F, Lundqvist M, Wannberg B, Mun B S, Hussain Z and Liu Z 2010 New ambient pressure photoemission endstation at Advanced Light Source beamline 9.3.2 *Rev. Sci. Instrum.* **81** 053106
[32] Chang R, Hong Y P, Axnanda S, Mao B H, Jabeen N, Wang S D, Tai R Z and Liu Z 2012 In-situ photoelectron spectroscopy with online activity measurement for catalysis research *Curr. Appl Phys.* **12** 1292–6
[33] Crumlin E, Liu Z, Bluhm H, Yang W, Guo J and Hussain Z 2015 X-ray spectroscopy of energy materials under in situ/operando conditions *J. Electron Spectrosc. Relat. Phenom.* **200** 264–73
[34] Qian J, Ye Y, Yang H, Yano J, Crumlin E and Goddard W 2019 Initial steps in forming the electrode-electrolyte interface: H2O adsorption and complex formation on the Ag(111) surface from combining quantum mechanics calculations and ambient pressure x-ray photoelectron spectroscopy *J. Am. Chem. Soc.* **141** 6946–54
[35] Zhang C J *et al* 2012 Multielement activity mapping and potential mapping in solid oxide electrochemical cells through the use of operando XPS *ACS Catal.* **2** 2297–304
[36] Zhu H, Ricote S, Coors W G, Chatzichristodoulou C and Kee R J 2014 Equilibrium and transient conductivity for gadolium-doped ceria under large perturbations: II. Modeling *Solid State Ion.* **268** 198–207
[37] Bond G C and Thompson D T 1999 Catalysis by gold *Catal. Rev. Sci. Eng.* **41** 319–88
[38] Graves C, Ebbesen S, Jensen S, Simonsen S and Mogensen M 2015 Eliminating degradation in solid oxide electrochemical cells by reversible operation *Nat. Mater.* **14** 239–44
[39] Wang L 2014 Model development for gadolinia-doped ceria-based anodes in solid oxide fuel cells *Ph.D Dissertation* (College Park, MD: Mechanical Engineering, University of Maryland) (https://doi.org/10.13016/M2FK6T)
[40] Wang L, Jackson G S and Blackburn B M 2013 Developing 3-D model of intermediate-temperature SOFC with GDC electrolyte *Solid Oxide Fuel Cells 13 (Sofc-Xiii)* **57** 2583–95
[41] Ioannidou E, Neofytidis C, Sygellou L and Niakolas D 2018 Au-doped Ni/GDC as an improved cathode electrocatalyst for H2O electrolysis in SOECs *App. Catal.* B **236** 253–64
[42] Zhu H Y, Kee R J, Janardhanan V M, Deutschmann O and Goodwin D G 2005 Modeling elementary heterogeneous chemistry and electrochemistry in solid-oxide fuel cells *J. Electrochem. Soc.* **152** A2427–40
[43] Shin H H and McIntosh S 2013 Insights into hydrogen oxidation on SOFC anode materials by isotopic exchange *ECS Electrochem. Lett.* **2** F88–91